

# A 7T fMRI dataset of synthetic images for out-of-distribution modeling of vision

Alessandro T. Gifford,<sup>1,2,3\*</sup> Radoslaw M. Cichy,<sup>1,2,3,4</sup>  
Thomas Naselaris,<sup>5,6</sup> Kendrick Kay<sup>5\*</sup>

<sup>1</sup> Department of education and Psychology, Freie Universität Berlin, Berlin, Germany

<sup>2</sup> Einstein Center for Neurosciences Berlin, Berlin, Germany

<sup>3</sup> Bernstein Center for Computational Neuroscience Berlin, Berlin, Germany

<sup>4</sup> Berlin School of Mind and Brain, Berlin, Germany

<sup>5</sup> Center for Magnetic Resonance Research, Department of Radiology, University of Minnesota, Minneapolis, MN, USA

<sup>6</sup> Department of Neuroscience, University of Minnesota, Minneapolis, MN, USA

\* Correspondence: [alessandro.gifford@gmail.com](mailto:alessandro.gifford@gmail.com), [kay@umn.edu](mailto:kay@umn.edu)

**Large-scale visual neural datasets such as the Natural Scenes Dataset (NSD) are boosting NeuroAI research by enabling computational models of the brain with performances beyond what was possible just a decade ago. However, these datasets lack out-of-distribution (OOD) components, which are crucial for the development of more robust models. Here, we address this limitation by releasing NSD-synthetic, a dataset consisting of 7T fMRI responses from the eight NSD subjects for 284 carefully controlled synthetic images. We show that NSD-synthetic's fMRI responses reliably encode stimulus-related information and are OOD with respect to NSD. Furthermore, OOD generalization tests on NSD-synthetic reveal differences between models of the brain that are not detected with NSD—specifically, self-supervised deep neural networks better explain neural responses than their task-supervised counterparts. These results showcase how NSD-synthetic enables OOD generalization tests that facilitate the development of more robust models of visual processing, and the formulation of more accurate theories of human vision.**

# Introduction

Recently, there has been an increase in both collection and use of large-scale visual neural datasets, suggesting that the field of vision science is entering a new era of big open data (1–7). One example of this recent trend in the context of human fMRI is the Natural Scenes Dataset (NSD) which provides high-quality 7T fMRI responses to over 70,000 images of naturalistic scenes across 8 subjects (1). Its unprecedented size and quality have made NSD one of the most popular go-to datasets for research in NeuroAI, where data-hungry machine- and deep-learning models are used to understand the functioning of the brain (8–13). Within three years since its release, NSD has been used in hundreds of research projects, leading to the development of state-of-the-art predictive models of neural responses to visual stimulation (14–16) and to new theory formation (17–21). Thus, large-scale visual neural datasets such as NSD are enabling new progress in computational models of the brain, leading to new theoretical insights.

However, it remains difficult to assess the level of out-of-distribution (OOD) generalization of brain models built using recent large-scale neural datasets, that is, whether model predictions generalize outside of the visual distribution on which they are trained (22). This is because, despite the unprecedented size of these datasets, their stimuli typically live within the same visual distribution, which comprises only a fraction of the vast visual space that our brains process during our lifetime. As a result, brain models are typically tested in-distribution (ID), that is, within the visual distribution on which they are trained. However, OOD tests are critical for intelligence research in three significant ways. First, successful models should predict brain responses under a broad range of situations. In that sense, OOD generalization serves as a stricter but essential assessment of model robustness and validity than ID tests. Poor OOD generalization indicates that theoretical inferences of brain function might not apply beyond stimuli from the train distribution, suggesting that further development is needed to capture stimulus-to-brain-response relationships. Second, breaking down generalization scores across different types of OOD conditions can reveal stimulus properties that neural models fail to account for (23), hence providing explicit targets for model improvement. Third, OOD generalization scores serve to distinguish among models that may otherwise have similar ID test scores (24, 25). Finding that one of several similarly-performing models generalizes better OOD can reveal important properties that make models successful (e.g., architecture, training diet, learning objective), informing the engineering of more robust models and inspiring new hypotheses about brain function.

To address the lack of OOD components in large-scale visual neural datasets and enable crucial OOD generalization tests of brain models, here we release a companion dataset to NSD called *NSD-synthetic* (for the remainder of the paper, we refer to NSD as *NSD-core*, to distinguish it from *NSD-synthetic*). *NSD-synthetic* consists of fMRI responses for an additional scan session from the same eight subjects of *NSD-core*. During this session, fMRI responses were measured to 284 carefully controlled synthetic (non-naturalistic) stimuli while the subject performed either a fixation task or a one-back task. Through computational analyses and modeling we show that *NSD-synthetic*'s fMRI responses reliably encode stimulus-related information, that the responses are out-of-distribution with respect to *NSD-core*, that encoding models trained on *NSD-core* generalize OOD on *NSD-synthetic* with lower prediction accuracies compared to ID generalization on *NSD-core*, and that OOD tests on *NSD-synthetic* reveal differences between encoding models not detected by ID tests on *NSD-core*. Together, as the OOD companion of *NSD-core*, *NSD-synthetic* enables strict OOD generalization tests critical for development of more robust models of visual processing and the formulation of more accurate theories of human vision.

# Results

## NSD-synthetic stimuli and experimental design



**Fig. 1. Stimuli and experimental design.** (A) Example natural scenes from NSD-core. (B) Example stimulus images in NSD-synthetic. The images are divided into 8 classes,

indicated by colored boxes. Every class is further divided into a varying number of subclasses, where each subclass consists of 4 images. For each subclass, we visualize one of the four images along with the subclass name. For visualization purposes, the images with the most peripheral words are not square cropped (Word4 Pos1, Word4 Pos5, Word6 Pos1, Word6 Pos5). **(C)** Trial design. Images were presented using a 2-s ON, 2-s OFF trial structure. A small central fixation dot changed luminance every 1.4 s. **(D)** Tasks. Subjects performed two different tasks in alternating runs. In the fixation task, subjects reported increments and decrements of the luminance of the fixation dot. In the one-back task, subjects judged whether the currently presented image was identical to the previously presented image.

In contrast to the natural scene stimuli in NSD-core (**Fig. 1A**), we created a set of 284 carefully controlled images divided into 8 classes. Every class contains multiple subclasses of 4 images each. The image classes include: various types of noise (4 subclasses, 16 images); natural scenes (2 subclasses, 8 images); manipulated version of natural scenes (3 subclasses, 12 images); contrast modulation (4 subclasses, 16 images); phase-coherence modulation (4 subclasses, 16 images); single words varying in position (10 subclasses, 40 images); spiral gratings varying in orientation and spatial frequency (28 subclasses, 112 images); and chromatic noise varying in hue (16 subclasses, 64 images) (**Fig. 1B**).

We presented these images in a rapid event-related design consisting of 4-s trials (2-s ON, 2-s OFF) while measuring fMRI responses (7T, 1.8-mm resolution) from each of the eight NSD subjects (**Fig. 1C**). To assess potential task dependence of neural responses, subjects performed a fixation task and a one-back task in alternating runs (**Fig. 1D**). In the fixation task, subjects reported brightness increments and decrements of the fixation dot. In the one-back task, subjects reported whether the current image was identical to the previous image. The subjects exhibited good behavioral compliance: overall percent correct in the fixation task was 98%, 97%, 80%, 94%, 97%, 92%, 76%, and 83%, and overall  $d'$  in the one-back task was 3.3, 2.6, 1.6, 2.7, 2.6, 3.2, 2.2, and 1.9. For the purposes of this paper, we pool fMRI responses across tasks and analyze fMRI responses with respect to the stimulus presented.

# NSD synthetic's fMRI responses reliably encode stimulus-related information

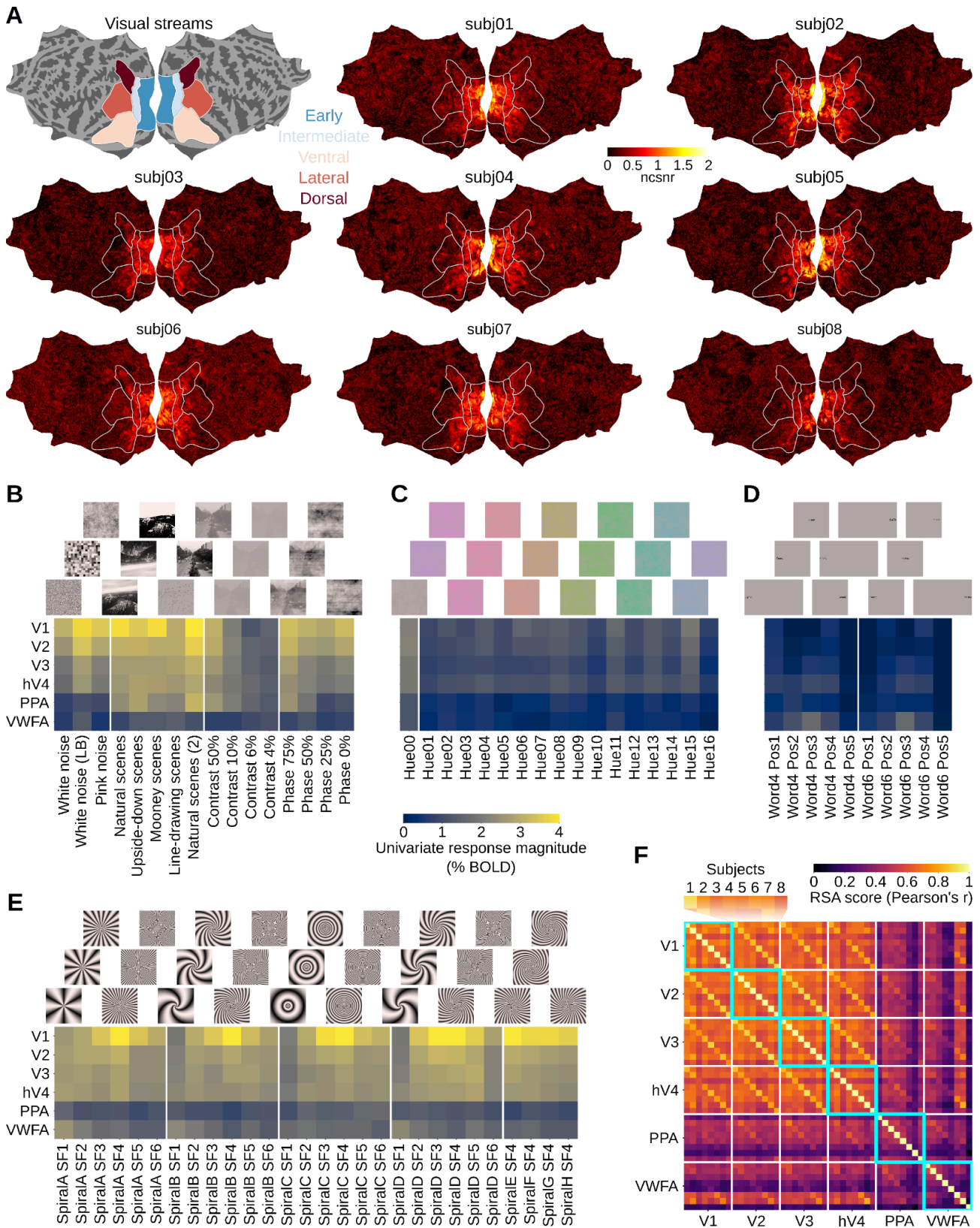


**Fig. 2. Noise ceiling, univariate, and multivariate analyses reveal robust visual signals in NSD-synthetic.** (A) Subject-wise noise ceiling signal-to-noise ratio (ncsnr), plotted on flattened cortical surfaces. White contours indicate regions based on the ‘streams’ ROI collection as provided in the NSD data release. (B) ROI-wise subject-average univariate responses for noise, natural/manipulated scenes, contrast modulation, and phase-coherence modulation (groupings indicated by vertical white lines). (C) ROI-wise responses for chromatic noise (Hue01–Hue16) and corresponding achromatic noise (Hue00). (D) ROI-wise responses for single words. For visualization purposes, the images with the most peripheral words are not square cropped (Word4 Pos1, Word4 Pos5, Word6 Pos1, Word6 Pos5). (E) ROI-wise responses for spiral gratings. (F) RSA scores indicating the similarity of multivariate fMRI responses between subjects and ROIs. Thin white lines separate groups of the eight subjects within the same ROI. Cyan boxes indicate cross-subject comparisons within the same ROI.

NSD-synthetic’s main purpose is to facilitate out-of-distribution (OOD) generalization tests aimed at improving the robustness of computational models of the brain. A prerequisite of these tests is that NSD-synthetic’s fMRI responses must reliably encode the different stimulus images. To assess this, we calculated NSD-synthetic’s noise ceiling signal-to-noise ratio (ncsnr), a measure of stimulus-related signal in the fMRI responses, using methods introduced in previous work (1). For all subjects, we found that ncsnr scores are high in and around visual cortex, ranging approximately from 0.75–2 (Fig. 2A). This indicates that 36–80% variance in single-trial responses reflects signals driven by the stimulus. Hence, stimulus-related information is indeed reliably encoded in NSD-synthetic’s fMRI responses. Within visual cortex, the ncsnr is highest in early areas compared to intermediate, ventral, dorsal, and lateral areas. We believe this reflects the limited visual and semantic complexity of NSD-synthetic’s stimuli, which leads to reduced signals in higher visual areas that preferentially respond to more complex visual features (26–31).

To further assess the quality of the encoded visual information, we next analyzed NSD-synthetic’s univariate and multivariate fMRI responses from both early visual cortex (EVC) and high-level visual cortex (HVC) regions of interest (ROIs). We chose ROIs based on their known responsiveness for the visual features defining NSD-synthetic’s stimulus images, so as to best characterize the visual information encoded in NSD-synthetic’s fMRI responses. The EVC ROIs consisted of V1, V2, V3, and hV4, due to their responsiveness to low- and mid-level visual features such as spatial frequency (32), contrast energy (33), edges (34), and color (35). The HVC ROIs consisted of the parahippocampal place area (PPA) due to its responsiveness to visual scenes (28) and of the visual word form area (VWFA) due to its responsiveness to visual words (36).

We begin by showing that NSD-synthetic’s univariate fMRI responses—defined as the average activity over all vertices within each ROI—for each image subclass reproduce known tunings of EVC and HVC ROIs. In Fig. 2B, we see that images of scenes activate PPA more than images consisting of noise, images with low contrast, and images with low phase-coherence, in line with PPA’s tuning to visual environments (28). Additionally, univariate responses increase substantially with increasing contrast for EVC ROIs (37). Finally, images consisting of noise and images with low phase coherence activate EVC ROIs more than HVC ROIs, in line with EVC’s selectivity for low-level visual features such as contrast energy (33). In Fig. 2C, we find that chromatic noise activates EVC more than HVC, in line with EVC’s role in the processing of color (35) and the fact that the chromatic noise patterns lack high-level structure. In Fig. 2D, we see that single words

activate VWFA the most, especially when presented foveally (i.e., Word4 Pos3, Word6 Pos3), in line with VWFA's tuning to visual words (36). In **Fig. 2E**, we see that spiral gratings activate EVC more than HVC, in line with EVC's general responsiveness to contrast energy (33). Among all EVC ROIs, V1 is driven by spiral gratings the most, and shows preferential tuning for certain spatial frequencies within each spiral grating type (e.g., 'SpiralA SF4', 'SpiralB SF4', 'SpiralC SF4') (38–40).

Next, we analyze the visual information in NSD-synthetic's multivariate fMRI responses—i.e., population response patterns over all vertices within each ROI. Through representational similarity analysis (RSA) (41), we assessed the similarity of multivariate fMRI responses between each subject and ROI. For each ROI, we found that NSD-synthetic's multivariate fMRI responses are correlated between subjects (RSA scores within the cyan boxes in **Fig. 2F**), indicating that subjects have shared visual representations. The cross-subject RSA scores are higher for EVC than for HVC, in line with the ncsnr and univariate response results indicating EVC ROIs are more responsive to NSD-synthetic's stimulus images than HVC ROIs (**Fig. 2A-E**). We also found that the multivariate fMRI responses are correlated between ROIs (RSA scores outside the cyan boxes in **Fig. 2F**), again more so for EVC ROIs. In particular, RSA scores from ROIs in the same subject are elevated (k-th subdiagonals in **Fig. 2F**), which may be indicative of spatial noise correlations shared across areas. However, the multivariate responses from different ROIs are also highly similar across subjects (off-subdiagonal entries in **Fig. 2F**). Since noise is uncorrelated between subjects, this bypasses the effect of spatial noise correlations and indicates similarity of visual representations across areas.

In summary, NSD-synthetic's fMRI responses reliably encode stimulus-related information with the strongest stimulus-driven responses occurring in EVC ROIs. The encoded information conforms to known tuning properties of EVC and HVC ROIs, and is consistent across subjects.

## NSD-synthetic's fMRI responses are out-of-distribution with respect to NSD-core

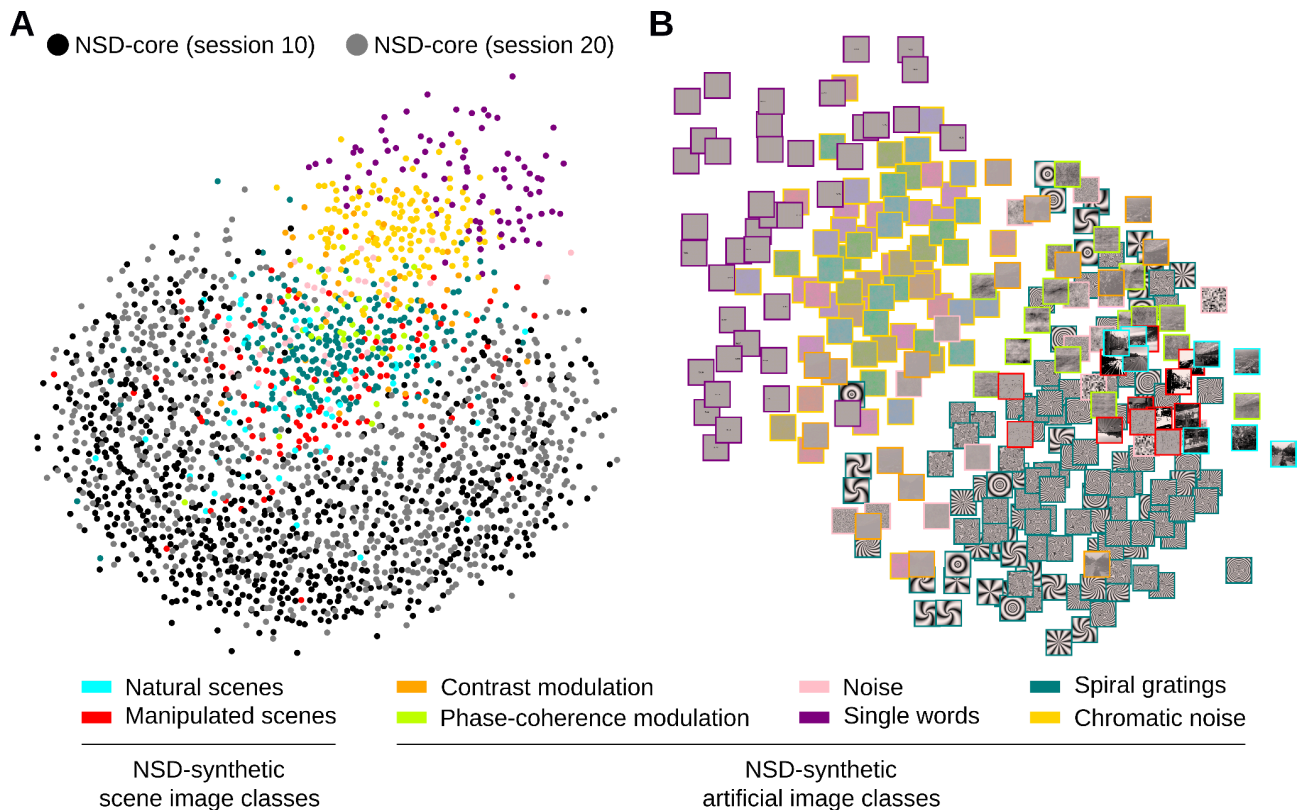


**Fig. 3. Multidimensional scaling (MDS) confirms brain responses to NSD-synthetic's artificial stimuli are out-of-distribution with respect to natural scenes.** (A) MDS embedding of single-trial fMRI responses from the NSD-synthetic scan session and two NSD-core scan sessions. Colored dots represent trials from the NSD-synthetic session, color-coded according to image class. Black and gray dots represent trials from two NSD-core sessions, respectively. (B) MDS embedding of trial-averaged fMRI responses to each of the 284 NSD-synthetic images. Colored borders indicate image class.

To be well suited for OOD generalization tests, NSD-synthetic's fMRI responses should not only reliably encode stimulus-related visual information, but should also exhibit a different distribution compared to NSD-core's responses. To ascertain this, we reduced NSD-synthetic and NSD-core's fMRI responses to two dimensions using multidimensional scaling (MDS) (42, 43), and compared the resulting two-dimensional MDS embeddings. To evaluate whether differences in distribution are due to unwanted session-specific effects, we applied MDS jointly on NSD-synthetic's single-trial fMRI responses and on the single-trial fMRI responses from two NSD-core scan sessions (sessions 10 and 20), aggregated across subjects. We found that the single-trial fMRI responses for NSD-synthetic form a distinct cluster compared to the single-trial fMRI responses from NSD-core (Fig. 3A). The fact that the single-trial fMRI responses from the two NSD-core scan sessions overlap in the MDS embedding space suggests that the difference between NSD-synthetic and NSD-core's data distributions is not driven by session effects, but rather by stimulus-related signals.



These two-dimensional MDS embeddings additionally revealed two clear patterns visible by eye. First, NSD-synthetic's responses for scene images are closer in the MDS embedding space to NSD-core (**Fig. 3A**), which is reasonable given that NSD-core consists of fMRI responses to scenes. Second, NSD-synthetic's fMRI responses cluster based on the image class to which they belong (**Fig. 3A**). To visualize this more effectively, we applied MDS on NSD-synthetic's trial-averaged fMRI responses for the 284 stimulus images only, and plotted these images positioned at the two-dimensional MDS embedding coordinates (**Fig. 3B**). Again, we see a clear clustering based on image classes. This clustering is consistent with properties of NSD-synthetic's stimulus images that are visible by eye, and is geometrically similar to the class clustering from applying MDS jointly on NSD-synthetic and NSD-core's responses (**Fig. 3A**).

In summary, NSD-synthetic's fMRI responses are differently distributed (i.e., OOD) with respect to NSD-core. These distributional differences are driven by the distinctness of NSD-synthetic's visual stimuli, and the similarity structure of NSD-synthetic's fMRI responses appears to mirror what is visible in the stimulus images.

# NSD-synthetic enables out-of-distribution generalization tests for deep neural network models of the brain

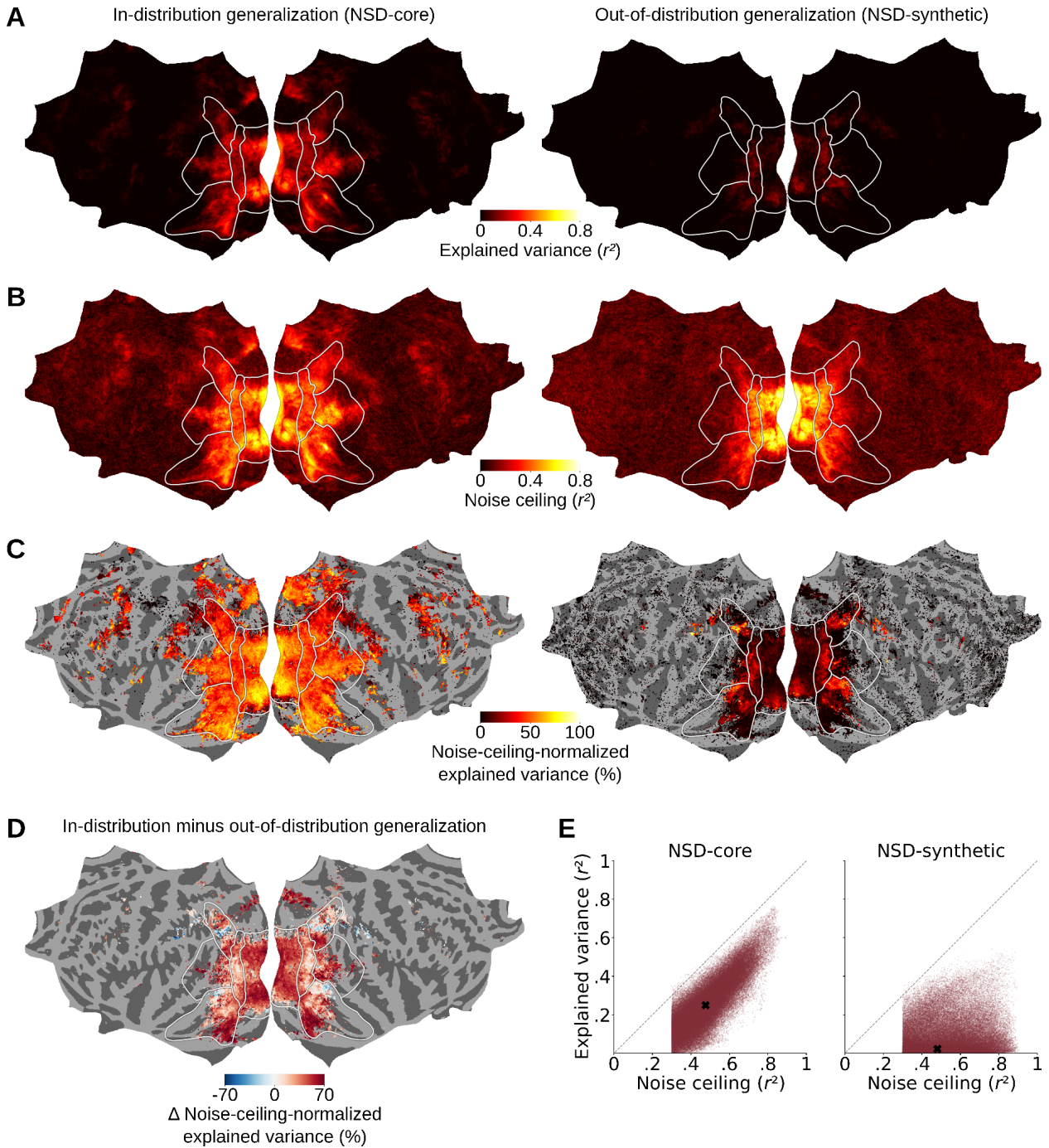


**Fig. 4. Brain encoding models exhibit reduced performance when tested out-of-distribution on NSD-synthetic.** We built deep-neural-network-based encoding models and tested them in-distribution (ID) on NSD-core as well as out-of-distribution (OOD) on NSD-synthetic. This figure shows results averaged across subjects on flattened cortical surfaces. **(A)** Model explained variance ( $r^2$ ). **(B)** Noise ceiling ( $r^2$ ). **(C)** Model explained variance normalized by the noise ceiling. To reduce false positives, for each vertex we averaged results from only those subjects with a noise ceiling greater than 0.3 (vertices for which no subject has a noise ceiling above 0.3 are not shown).

(D) Difference between ID and OOD noise-ceiling-normalized explained variance. For each vertex, we averaged results from only those subjects with noise ceiling greater than 0.3 for both NSD-core and NSD-synthetic. (E) Scatterplots of vertex-wise explained variance scores against their noise ceilings for ID (NSD-core) and OOD (NSD-synthetic) generalization tests. For each vertex, we plotted results from only those subjects with noise ceiling greater than 0.3 for both NSD-core and NSD-synthetic (same as in panel D). Black crosses indicate median scores across all vertices.

Having established that NSD-synthetic is OOD with respect to NSD-core, we turn to assessing whether NSD-synthetic is useful for OOD generalization tests of computational models of the brain. As computational models we used neural encoding models, that is, predictive algorithms that generate brain responses to arbitrary stimulus images (13, 44–47). We hypothesized that encoding models trained on NSD-core would generalize OOD on NSD-synthetic with lower prediction accuracies than they would for ID generalization.

The encoding models consisted of linear regressions that map image features onto the fMRI responses of each vertex. For image features we used the activations of AlexNet (48), a convolutional neural network pretrained on image classification that is a well-established standard in computational visual neuroscience research. We trained the linear regression weights using image features and fMRI responses from NSD-core, and tested their generalization performance both ID and OOD. For ID tests, we used a separate data partition of NSD-core not used for model training; for OOD tests, we used NSD-synthetic. We quantified generalization performance by correlating the predicted fMRI responses with their recorded (i.e., experimentally collected) counterparts, obtaining ID and OOD explained variance scores for each subject and vertex (Fig. 4A). Critically, explained variance scores are determined not only by the encoding model's generalization performance, but also by the level of noise in the recorded fMRI responses (which might differ between the ID and OOD fMRI responses). Thus, to make the ID and OOD explained variance scores more meaningful and directly comparable, we normalized them with the noise ceiling of the corresponding recorded fMRI responses (Fig. 4B). This resulted in ID and OOD noise-ceiling-normalized explained variance scores that indicate the amount of explainable variance accounted for by the models for each vertex and subject (Fig. 4C).

We found that the encoding models trained on NSD-core predict visual fMRI responses better ID than OOD (Fig. 4C-D). The fact that OOD generalization is lower is crucial, as it indicates that further improvement is needed to capture stimulus-to-brain-response relationships, thus validating NSD-synthetic's usefulness for model and theory development. We further observed that decreases in OOD performance compared to ID performance are consistent across both lower- and higher-level visual areas (see red regions in Fig. 4D). Importantly, these decreases in performance are not due to lack of explainable signal in NSD-synthetic's fMRI responses, but rather to model failures. When plotting the vertex-wise explained variance scores against their noise ceilings, we found that compared to ID tests on NSD-core, the encoding models' explained variance scores were consistently lower relative to the noise ceiling for OOD tests on NSD-synthetic (Fig. 4E).

In summary, we showed that encoding models trained on NSD-core generalize ID and, to a lower extent, OOD on NSD-synthetic. The lower OOD generalization performance opens the door for using NSD-synthetic in combination with NSD-core to perform OOD generalization tests for model and theory improvement.

# Out-of-distribution generalization tests reveal differences between brain models not detected by in-distribution tests

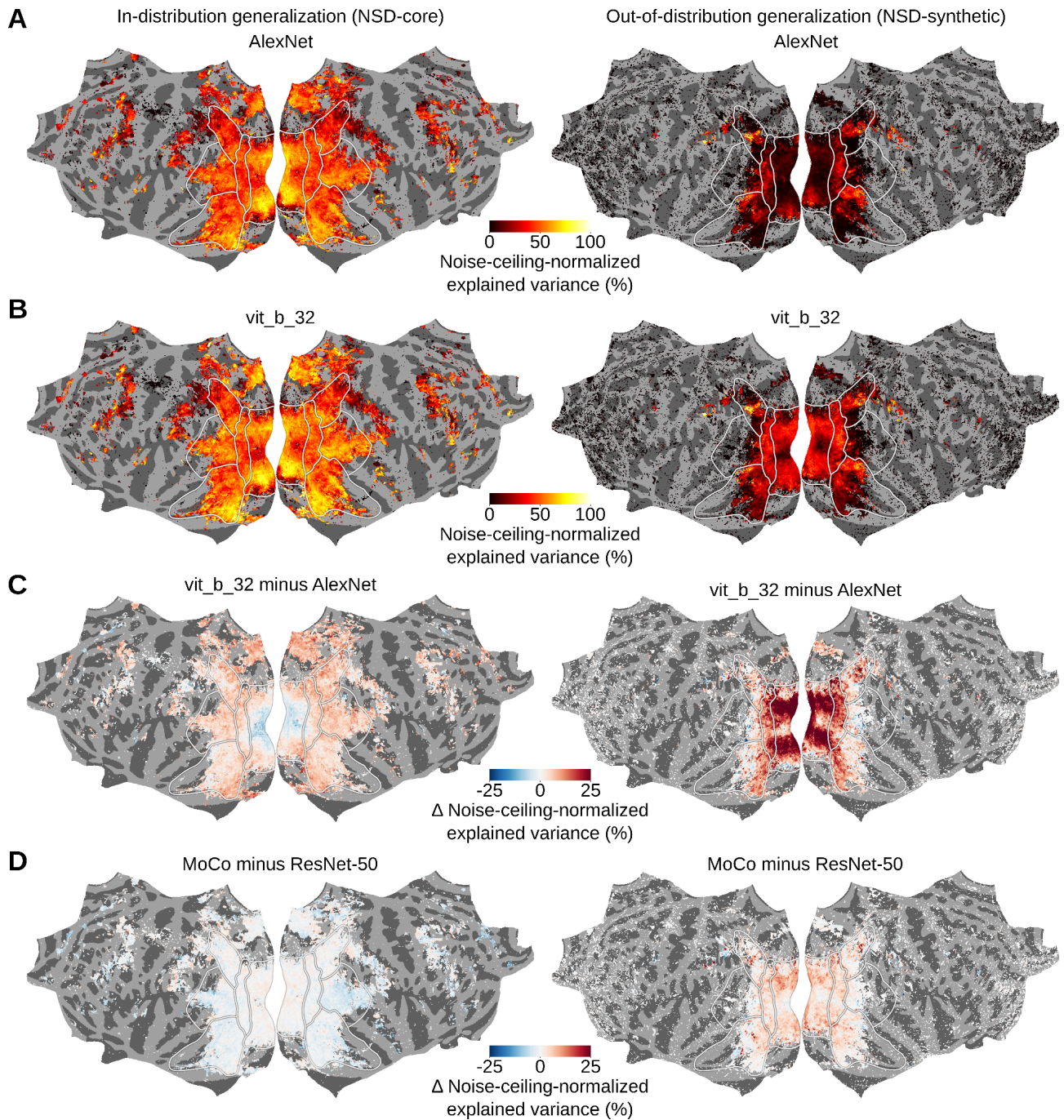


**Fig. 5. Out-of-distribution generalization tests reveal differences between brain encoding models not detected by in-distribution tests.** We built deep-neural-network-based encoding models and tested them in-distribution (ID) on NSD-core as well as out-of-distribution (OOD) on NSD-synthetic. This figure shows results averaged across subjects on flattened cortical surfaces. To reduce false positives, for each vertex we averaged results from only those subjects with a noise ceiling greater than 0.3 (vertices for which no subject has a noise ceiling above 0.3 are not shown). **(A)** AlexNet encoding models' explained variance normalized by the noise

ceiling. **(B)** vit\_b\_32 encoding models' explained variance normalized by the noise ceiling. **(C)** Difference between AlexNet and vit\_b\_32's noise-ceiling-normalized explained variance. **(D)** Difference between MoCo and ResNet-50's noise-ceiling-normalized explained variance.

After demonstrating that NSD-synthetic enables OOD generalization tests, we finally ask whether these tests reveal differences between brain models that are not detected by ID tests. If so, NSD-synthetic would provide unique insight essential for developing more robust models of the brain.

To assess this, we compared the ID and OOD noise-ceiling-normalized explained variance scores of AlexNet-based encoding models (**Fig. 5A**), with the scores of encoding models based on a more modern computer vision architecture, a vision transformer pretrained on image classification called vit\_b\_32 (49) (**Fig. 5B**). When tested ID, we found that AlexNet outperformed vit\_b\_32 in lower-level visual areas (blue areas in **Fig. 5C**, left panel), and that vit\_b\_32 outperformed AlexNet in higher-level visual areas (red areas in **Fig. 5C**, left panel). This ID difference between the two models was modest, peaking at 10% of absolute explained variance difference (**Fig. 5C**, left panel). Surprisingly, when testing the models OOD we found that vit\_b\_32 instead outperformed AlexNet across both lower- and higher-level visual areas (red areas in **Fig. 5C**, right panel). This OOD difference between the two models was much stronger than their ID difference, peaking at 25% of absolute explained variance difference (**Fig. 5C**, right panel). Thus, OOD tests revealed differences between brain models not detected by ID tests. These differences suggest that vit\_b\_32 is a more robust model of visual cortex compared to AlexNet. Furthermore, the magnitudes of absolute explained variance difference scores indicate that OOD tests allow to better disentangle brain models compared to ID tests.

In a last comparison, we assessed whether OOD tests reveal unique differences also between brain encoding models based on highly similar deep neural networks. Specifically, we compared encoding models based on ResNet-50 (50), a recurrent convolutional neural network pretrained on task-supervised image classification, with encoding models based on MoCo (51), consisting of the same ResNet-50 architecture but trained with self-supervised contrastive learning (52). When tested ID, we found that ResNet-50 outperformed MoCo in higher-level visual areas (blue areas in **Fig. 5D**, left panel), and that MoCo outperformed ResNet-50 in lower-level visual areas (red areas in **Fig. 5D**, left panel). When tested OOD, MoCo instead outperformed ResNet-50 across both lower- and higher-level visual areas (red areas in **Fig. 5D**, right panel). The ID difference between the two models was smaller (peaking at 5% of absolute explained variance difference, **Fig. 5D**, left panel) compared to their OOD difference (peaking at 10% of absolute explained variance difference, **Fig. 5D**, right panel), again indicating that OOD tests allow to better disentangle brain models compared to ID tests. Thus, OOD tests reveal differences not detected by ID tests also for encoding models based on highly similar deep neural networks. These differences suggest that self-supervised deep neural networks are more robust models of visual cortex compared to task-supervised ones.

In conclusion, we found that OOD tests reveal differences between models that are not detected ID. This indicates that the outcomes of OOD and ID generalization tests do not imply one another, and therefore that NSD-synthetic provides unique insight for model development.

# Discussion

Here we release NSD-synthetic, the out-of-distribution (OOD) companion dataset of NSD-core. We have shown that NSD-synthetic's fMRI responses have high signal-to-noise ratio and reliably encode properties of the presented visual stimuli (**Fig. 2**). Importantly, we have also demonstrated that the distribution of visually evoked responses in NSD-synthetic are fundamentally different compared to the distribution of visually evoked responses in NSD-core (**Fig. 3**), that encoding models trained on NSD-core generalize to NSD-synthetic with lower prediction accuracies than they do to NSD-core (**Fig. 4**), and that OOD tests on NSD-synthetic reveal differences between models that are not detected by in-distribution tests on NSD-core (**Fig. 5**). Together, these findings successfully establish NSD-synthetic as a useful out-of-distribution companion to NSD-core. All data are publicly available, including data in ready-to-use preprocessed formats, at <http://naturalscenesdataset.org>. We hope researchers will take advantage of this new dataset in building more robust and accurate computational models of the brain, leading to better theories of vision.

## The importance of out-of-distribution tests for robust models and accurate theories of vision

OOD generalization refers to modeling scenarios where the test data distribution differs from the train data distribution, resulting in stricter tests of model robustness compared to in-distribution (ID) tests (22). In line with this, we found that NSD-synthetic's fMRI responses are indeed distributed differently than NSD-core's responses, and that encoding models trained on NSD-core achieve lower generalization performance when tested OOD on NSD-synthetic. Finding a lower OOD generalization performance is essential for establishing NSD-synthetic as a stricter testbed that highlights deficiencies of brain models not observable with ID tests.

Beyond indicating that further model improvement is required to accurately describe visual representations in the brain, NSD-synthetic also suggests directions for closing the gap between ID and OOD generalization performance. One direction of model improvement comes from consideration of the properties of NSD-synthetic's stimuli. Since the stimuli consist of a multitude of diverse and carefully parameterized images, they facilitate discovery of the specific OOD visual features to which computational models fail to generalize, which in turn provide explicit objectives for the engineering of more robust models (23, 53). Another direction of model improvement comes from benchmarking the performance of different computational models on NSD-synthetic and isolating model properties leading to best OOD generalization (24, 25). Because each model embeds a different hypothesis of visual processing, these OOD generalization tests can help adjudicate between competing hypotheses, therefore facilitating theory formation.

As an example of this, we found that encoding models based on self-supervised deep neural networks better generalize OOD than encoding models based on their task-supervised counterparts, in line with recent work proposing self-supervision as a more plausible account of coding in visual cortex (54, 21, 55). As another illustrative example, St-Yves and colleagues used NSD-synthetic to compare OOD generalization between encoding models with or without hierarchical visual representations. They found that non-hierarchical representations most accurately predict NSD-synthetic's fMRI responses, whereas the difference between non-hierarchical and hierarchical models was much less apparent when testing predictions ID on

NSD-core. Based on these findings, the authors derived the theoretical conclusion that “*instead of forming a serial processing cascade that supports a single function, the diverse representations in V1–V4 may subserve diverse and independent functions that are distributed across the visual areas*” (20).

## Considerations in conducting out-of-distribution generalization tests

To obtain valid inferences, the details, quantifications, and interpretation of OOD tests require careful consideration. Here, we comment on two specific issues that researchers should consider when performing OOD generalization tests on NSD-synthetic.

First, we interpreted the distributional differences between NSD-synthetic and NSD-core’s fMRI responses as stemming from differences in the stimuli of the two datasets. However, in theory, distributional differences might also reflect other properties of the data, such as differences in task (56), session-specific effects, and fluctuations in cognitive state. All these data properties represent diverse dimensions across which different datasets might fall in- or out-of-distribution. Therefore, to improve transparency, reproducibility, and comparison across studies using NSD-synthetic, we recommend researchers to explicitly define the OOD operationalization used.

Second, properties of the data not relevant to the researcher’s question of interest might introduce spurious distributional differences between NSD-synthetic and NSD-core’s fMRI responses. For example, the trial timing differed between NSD-core (3-s ON, 1-s OFF) and NSD-synthetic (2-s ON, 2-s OFF), with longer image onscreen times typically leading to higher fMRI responses (57). Additionally, since NSD-synthetic and NSD-core’s fMRI responses come from distinct scan sessions, they are affected by session effects, that is, differences in fMRI responses across sessions due to incidental session-specific factors (e.g., time of day, arousal, cognitive state, hardware state). To eliminate spurious distributional differences, researchers might consider z-scoring fMRI responses within each scan session. However, by centering responses and transforming them to unit variance, z-scoring also alters the signal of interest, potentially eliminating distributional differences of interest. Our approach for compensating for differences in fMRI response gain due to trial timing was to quantify encoding model performance using Pearson correlation (which is insensitive to gain differences). Additionally, to reduce session effects we analyzed fMRI responses aggregated across subjects and considered vertices with a signal-to-noise ratio score above a certain threshold (see Methods).

## Comparison of NSD-synthetic to other out-of-distribution datasets

There are other large-scale visual fMRI datasets that have OOD components. One such OOD component comes from the Algonauts Project 2025 challenge dataset (58, 59) which consists of fMRI responses to multimodal movies including visual, auditory and linguistic stimulation. In this dataset, the test split was chosen to be OOD compared to the train split based on different movie dimensions (e.g., emotional valence, movie genre, language, background music, visual style). NSD-synthetic complements this dataset by offering fMRI responses from a carefully controlled stimulus set and experimental design (controlled artificial images presented sequentially while subjects maintained central fixation and performed two different tasks vs. uncontrolled naturalistic multimodal movies presented while subjects freely performed eye movements without an explicit task). In addition, NSD-synthetic provides fMRI responses at higher magnetic field strength (7T vs.

3T) and with twice as many subjects (8 vs. 4), though the Algonauts 2025 dataset does include more hours of fMRI data per subject.

Other large-scale fMRI datasets with OOD components include the Deep Image Reconstruction dataset (60) and the Visual Illusion Reconstruction dataset (61). These datasets consist of fMRI responses to naturalistic images of objects and scenes (ID component), as well as to artificial images, letters, and illusory images (OOD component). NSD-synthetic complements these datasets with fMRI responses for a different and larger set of OOD stimulus images (284 images vs. 50 or 38 for the Deep Image Reconstruction or Visual Illusion Reconstruction datasets, respectively). In addition, NSD-synthetic provides fMRI responses at higher magnetic field strength (7T vs. 3T) and a larger ID component on which to train computational models of the brain (up to 30,000 trials per subject in NSD-core vs. up to 7,200 or 16,000 trials per subject for the Deep Image Reconstruction or Visual Illusion Reconstruction datasets, respectively).

Overall, we emphasize that a key feature of NSD-synthetic is that it was conducted in concert with NSD-core. Over the last three years, NSD-core has become the most widely used dataset in computational visual neuroscience and a de-facto benchmark for NeuroAI research. Hence, there are exciting opportunities for enriching the insights derived from NSD.

## Other uses of the NSD-synthetic dataset

While NSD-synthetic's main strength is to enable OOD generalization tests, the dataset is also suitable for other use cases. First, it contains several well-controlled image manipulations that enable characterization of how specific visual dimensions affect brain responses (independent of any computational model). For example, NSD-synthetic stimuli allow an examination of whether and how neural representations differ when viewing a natural scene upside-down (62), viewing a binarized version of the scene (63), or viewing a line drawing of the scene (64, 65). Second, it contains fMRI responses across two different visual tasks: a fixation task where subjects reported increments and decrements of the luminance of the fixation dot and a one-back task where subjects judged whether the currently presented image was identical to the previously presented image. Given that the same stimuli were presented across the two tasks, these data allow investigation of whether and how cognitive tasks influence neural representations (56).

## Limitations of NSD-synthetic

The results of our analyses indicate that stimulus-related information in NSD-synthetic's fMRI responses is primarily encoded in early to intermediate visual cortical areas (i.e., V1 to hV4). This presumably is due to the fact that NSD-synthetic stimuli consist mostly of simple visual features that well activate early to intermediate visual cortex (e.g., various forms of noise and spiral gratings), but which are not well suited for driving activity in higher visual cortical areas responsive to perceptually and semantically more complex stimuli (26–31). Because of this, NSD-synthetic might be best suited for testing the OOD generalization of computational models of lower visual cortical areas.



# Materials and Methods

Procedures for data acquisition, data pre-processing, and GLM analysis were the same as in NSD-core. For full details of these procedures, please refer to NSD-core's paper (1). Below, we provide a detailed summary of the procedures.

## Subjects

The NSD-synthetic experiment was conducted with the same set of eight subjects who took part in NSD-core. These subjects (subj01–subj08) were right-handed with normal or corrected-to-normal visual acuity and no color blindness, and consisted of two males and six females, with age range 19–32 years. Informed written consent was obtained from all subjects, and the experimental protocol was approved by the University of Minnesota Institutional Review Board.

## MRI data acquisition

MRI data were collected at the Center for Magnetic Resonance Research at the University of Minnesota. Functional MRI data were collected using a 7T Siemens Magnetom passively shielded scanner and a single-channel-transmit, 32-channel-receive RF head coil (Nova Medical). Data for NSD-synthetic were collected in one scan session that took place after completion of the NSD-core experiment. The fMRI data were collected using gradient-echo EPI at 1.8-mm isotropic resolution with whole-brain coverage (84 axial slices, slice thickness 1.8 mm, phase encode direction anterior-to-posterior, TR 1,600 ms, TE 22.0 ms, partial Fourier 7/8, iPAT 2, multi-band slice acceleration factor 3). In addition to the EPI scans, the scan session also included dual-echo fieldmaps for post hoc correction of EPI spatial distortion (same overall slice slab as the EPI data, 2.2 mm × 2.2 mm × 3.6 mm resolution, TE1 8.16 ms, TE2 9.18 ms). The acquisition structure for the NSD-synthetic scan session was [F XOXO F XOXO F], where F indicates a fieldmap, X indicates a fixation run (268 TRs), and O indicates a one-back run (268 TRs).

## Stimulus display and scanner peripherals

Stimuli were presented using a Cambridge Research Systems BOLDscreen 32 LCD monitor positioned at the head of the 7T scanner bed. The monitor operated at a resolution of 1,920 pixels × 1,080 pixels at 120 Hz. Subjects viewed the monitor via a mirror mounted on the RF coil. The size of the monitor image was 69.84 cm (width) × 39.29 cm (height), and the viewing distance was 176.5 cm. Measurements of display spectral power density were obtained using a PR-655 spectroradiometer (Photo Research). A Mac Pro computer controlled stimulus presentation using code based on Psychophysics Toolbox 3.0.14. Behavioral responses were recorded using a button box (Current Designs). Ear plugs were used to reduce acoustic noise, and head motion was mitigated using headcases.

Eye-tracking was performed using an EyeLink 1000 system (SR Research). We caution that the eye-tracking data are variable in quality due to difficulties achieving sufficient pupil contrast in some subjects. In addition, eye-tracking data for the first NSD-synthetic run for subj05 were corrupted and are therefore not available. For full details of eye-tracking acquisition and pre-processing, see NSD-core's paper (1). Overall, we found that subjects were generally able to maintain good central

fixation during our various fMRI experiments, with the possible exception of subj05 (see NSD-core's Extended Data Fig. 4 (1)).

## The NSD-synthetic experiment

### Stimuli

Stimuli consisted of 284 distinct images. All images were presented under two different tasks, a fixation task and a one-back task. A high-level description of the images is as follows (the number of images is indicated in parentheses): white noise (4), white noise with a large block size (4), pink noise (4), natural scenes (4), upside-down versions of these scenes (4), Mooney versions of these scenes (4), line-drawing versions of these scenes (4), contrast-modulated natural scenes (4 scenes  $\times$  5 contrast levels (100%, 50%, 10%, 6%, 4%) = 20), phase-coherence-modulated natural scenes (4 scenes  $\times$  4 coherence levels (75%, 50%, 25%, 0%) = 16), single words (2 word lengths  $\times$  5 positions  $\times$  4 words = 40), spiral gratings varying in orientation and spatial frequency (112), and chromatic pink noise varying in hue (68).

Images were prepared at a resolution of 1,360 pixels (width)  $\times$  714 pixels (height), corresponding to a visual field extent of  $16^\circ \times 8.4^\circ$ . Most images occupy the central  $8.4^\circ \times 8.4^\circ$ , which is the stimulus size used in NSD-core; a few word stimuli extend beyond this central region (details below). Of the 284 images, the first 220 images are achromatic. Pixel luminance values for these images were prepared in the range 0–1 and then transformed using a color lookup table that increases linearly in luminance (L+M) with the chromaticity of D65. In this lookup table, the RGB values corresponding to the minimum and maximum luminance are (0,0,0) and (252,220,216), respectively. The remaining 64 images are chromatic, and their design is described in further detail below.

The images are hierarchically organized: there are 284 distinct images belonging to 71 image subclasses, and these 71 image subclasses belong to 8 image classes (Noise, Natural scenes, Manipulated scenes, Contrast modulation, Phase-coherence modulation, Single words, Spiral gratings, and Chromatic noise). Below, we describe each of the image subclasses. The parentheses at the end of each description indicates the associated image class.

*White noise: Image subclass 1 (images 1–4).* Each image consists of pixels whose luminance values were randomly drawn from a uniform distribution between 0–1. Four distinct images were generated. (Noise)

*White noise (large block): Image subclass 2 (images 5–8).* Pixels are grouped into block sizes of 42 pixels  $\times$  42 pixels ( $0.49^\circ \times 0.49^\circ$ ). Luminance values for each block were randomly drawn from a uniform distribution between 0–1. Four distinct images were generated. (Noise)

*Pink noise: Image subclass 3 (images 9–12).* Images with  $1/f$  amplitude spectra were generated. This was achieved by multiplying white Gaussian noise by the desired amplitude spectrum. For each image, pixel values from 3.5 standard deviations below and above the mean were linearly mapped to the range 0–1. Four distinct images were generated. (Noise)

*Natural scenes: Image subclass 4 (images 13–16).* Four natural scenes were chosen from the stimulus set used in a previous study (64); the motivation for choosing from this stimulus set is that the natural scenes have associated line drawings (which are used in image subclass 7). The four chosen scenes depict mountains, a highway, a street, and a desk. Each natural scene was converted to grayscale, square cropped, resized to 714 pixels × 714 pixels, converted to luminance values assuming a display gamma of 2.0, and then contrast-normalized such that the 0.1 and 99.9 percentiles were linearly mapped to the range 0–1. (Natural scenes)

*Upside-down scenes: Image subclass 5 (images 17–20).* The prepared images from image subclass 4 were rotated by 180°. (Manipulated scenes)

*Mooney scenes: Image subclass 6 (images 21–24).* We binarized the prepared images from image subclass 4 by thresholding each image at the median pixel value. The resulting images have pixel values of either 0 (black) or 1 (white), and are akin to Mooney images (63). Subjects were not explicitly pre-exposed to the intact versions of the images, but were presumably familiarized with the intact images over the course of the scan session. (Manipulated scenes)

*Line-drawing scenes: Image subclass 7 (images 25–28).* The line drawings associated with the natural scenes used in image subclass 4 were square cropped, resized to 714 pixels × 714 pixels, and then prepared as black lines (0) on a gray background (0.5). (Manipulated scenes)

*Natural scenes (second set): Image subclass 8 (images 29–32).* A second set of four natural scenes were chosen from the stimulus set used in the previous study (64). The four chosen scenes depict a forest, a superhighway, a boulevard, and cubicles. The same image preparation procedures were applied as in image subclass 4. (Natural scenes)

*Contrast 50%, Contrast 10%, Contrast 6%, Contrast 4%: Image subclasses 9–12 (images 33–48).* The prepared images from image subclass 8 were manipulated to have contrast levels of 50%, 10%, 6%, and 4%. This was achieved by designating the prepared images as having a contrast level of 100% and by scaling pixel luminance values towards 0.5 by the appropriate amount. (Contrast modulation)

*Phase 75%, Phase 50%, Phase 25%, Phase 0%: Image subclasses 13–16 (images 49–64).* We took the prepared images from image subclass 9 (the 'Contrast 50%' subclass) and manipulated the phase coherence level. Specifically, the phase spectrum of each image was blended with a random phase spectrum (e.g., 'Phase 75%' indicates a blend of 75% original and 25% random). A different random phase spectrum was used for each image and each coherence level. Pixel luminance values were then truncated to fit the range 0–1 (only a very small amount of clipping occurred). (Phase-coherence modulation)

*Word4 Pos1–5, Word6 Pos1–5: Image subclasses 17–26 (images 65–104).* Each image contains a single word (black on a gray background) written in a sans-serif, monospaced font (Liberation Mono). Half of the words are 4 letters long and presented in a relatively large font size (x-height 0.4°, center-to-center spacing 0.43°, word bounding box height 0.69°), and half of the words are 6 letters long in a smaller font size (x-height 0.27°, center-to-center spacing 0.28°, word bounding box height 0.46°). The 4-letter words roughly match the 6-letter words in horizontal extent (average word width 1.64°). The 4- and 6-letter words (20 in each set) are closely matched in lexical frequency. The words span a wide range of syntactic categories (parts of speech). Each word was

placed at one of five possible positions along the horizontal meridian ( $-6^\circ$ ,  $-3^\circ$ ,  $0^\circ$ ,  $3^\circ$ ,  $6^\circ$ ). For each combination of word length and position, four images were generated, yielding a total of 2 word lengths  $\times$  5 positions  $\times$  4 words = 40 images. Note that the words positioned at  $-6^\circ$  and  $6^\circ$  are the only images (out of the 284 NSD-synthetic images) with content that lies outside of the central  $8.4^\circ \times 8.4^\circ$  region. We caution that models trained on NSD-core may generalize poorly to these images due to their relatively peripheral image content. (Single words)

*SpiralA–D SF1–6, SpiraleE–H SF4: Image subclasses 27–54 (images 105–216).* These images are sinusoidal gratings in log-polar coordinates (we refer to these as ‘spiral gratings’ but they can also be called ‘log-polar gratings’). The primary advantage of spiral gratings over conventional Cartesian sinusoidal gratings is that for spiral gratings, spatial frequency varies inversely with eccentricity, thereby enabling more efficient sampling of neural tuning preferences (neurons at higher eccentricities are tuned for lower spatial frequencies) (66). We created spiral gratings at full contrast. We prepared four types of spirals, SpiralA–D (pinwheels, forward spirals, annuli, reverse spirals), at six spatial frequency levels ( $L = 6.0, 11.0, 20.0, 37.0, 69.0, 128.0$ ), and we prepared four additional types of spirals, SpiraleE–H (various intermediate spirals), at one spatial frequency level ( $L = 37.0$ ). For a given point in the visual field with eccentricity  $E$  (in degrees), the local spatial frequency (in cycles per degree) is given by  $L/(2\pi E)$ ; hence, for a fixed spatial frequency level  $L$ , different spirals have identical local spatial frequency content (but differ in local orientation). To avoid aliasing, a central circle was cut out of each image. The diameter of this circle was 4, 8, 14, 26, 48, and 86 pixels ( $0.05^\circ, 0.09^\circ, 0.16^\circ, 0.31^\circ, 0.56^\circ, \text{ and } 1.01^\circ$ ) for the six spatial frequency levels, respectively. We generated a total of 4 types of spirals (SpiralA–D)  $\times$  6 spatial frequency levels + 4 types of spirals (SpiraleE–H)  $\times$  1 spatial frequency level = 28 image subclasses. For each image subclass, four images were generated, corresponding to four equally spaced grating phases. Hence, the total number of images was 28 image subclasses  $\times$  4 phases = 112 images. For general information about the design of spiral gratings, please see this previous study (66). (Spiral gratings)

*Hue00: Image subclass 55 (images 217–220).* These images are the same as the prepared images from image subclass 3 (pink noise with  $1/f$  amplitude spectra) but lowered in contrast. The images are metameric in chromaticity with standard illuminant D65. Four images were generated. (Noise)

*Hue01–16: Image subclasses 56–71 (images 221–284).* These 64 images are the only chromatic images in NSD-synthetic. To create these images, we selected 16 different hues by choosing evenly spaced angles in a version of the MacLeod-Boynton chromaticity diagram (67) that is based on the Stockman, MacLeod, and Johnson cone fundamentals (68). We then determined the maximum saturation by fitting a circle with the maximum available radius within the gamut of the BOLDscreen display. Finally, for each hue, we created isoluminant images by taking the 4 pink noise patterns from image subclass 55 and using these patterns to modulate between zero saturation (the D65 gray point) and maximum saturation (within the determined circle). To ensure isoluminance for individual observers, we created participant-specific versions of the 64 images based on heterochromatic flicker photometry results obtained from each participant. (Chromatic noise)

For most image subclasses (comprising a total of 268 images), images naturally come in groups of four for which we do not expect much variation in brain activity. For example, for the ‘White noise’

subclass, the four generated images are quite similar to each other (they are just different samples of noise). As another example, for the 'SpiralA SF1' subclass, the four generated images differ only with respect to the specific phase of the underlying spiral grating. Hence, for these image subclasses, we present images only once per task (with the four presentations serving as quasi-repetitions). In contrast, for the 'Natural scenes', 'Upside-down scenes', 'Mooney scenes', and 'Line-drawing scenes' subclasses (comprising a total of 16 images), each distinct scene might be expected to produce a substantially different brain activity pattern. Hence, for these image subclasses, we present images four times per task. Overall, for a complete set of trials for one task, we require  $268 \text{ images} \times 1 \text{ presentation} + 16 \text{ images} \times 4 \text{ presentations} = 332 \text{ stimulus trials}$ .

## Trial and run design

Each trial lasted 4 s and consisted of the presentation of an image for 2 s, followed by a 2-s gap. (The motivation for the shorter 2-s duration compared to the 3-s duration in NSD-core was to reduce the strong adaptation effects caused by gratings.) In total, 107 trials were conducted in a run; thus, each run lasted 428 s. The first three trials (12 s) and the last four trials (16 s) were blank trials. The remaining 100 trials were divided into 93 stimulus trials and seven blank trials. The blank trials were randomly positioned in each run such that the minimum and maximum number of continuous stimulus trials was nine trials (36 s) and 14 trials (56 s), respectively.

We allocated four runs to complete the data for the fixation task. To determine trial ordering for these four runs, we first created a random ordering of the complete set of 332 stimulus trials, splitting these trials into 4 runs (83 stimulus trials each). This random ordering was subject to the constraint that no image was repeated back-to-back within a run. Then, for each run, we randomly selected 10 of the stimulus trials to be repeated as one-back trials. This yielded, for each run, a total of 83 regular stimulus trials + 10 inserted one-back trials = 93 stimulus trials.

A total of eight runs were collected in the NSD-synthetic scan session, with subjects alternating between the fixation task and the one-back task. To ensure that differences in brain activity across tasks are not due to stimulus-related differences, we took the run design for the fixation task and used it identically for the one-back task (albeit changing the run order). Specifically, the tasks performed in the eight runs were XOXOXOXO where X indicates the fixation task and O indicates the one-back task, and the run designs for the eight runs were ACBDCADB where A, B, C, and D correspond to the four runs designed for the fixation task (as described above). All stimulus and experiment characteristics (e.g., trial ordering, one-back events, dot color changes) were kept identical across subjects.

## Stimulus presentation and task

The BOLDscreen monitor was configured to behave as a linear display device, and all stimuli were delivered using a linear color lookup table. (For natural scene stimuli, we prepared the luminance of these stimuli to simulate standard display gamma; see details above.) Stimuli occupied  $16.0^\circ$  (width)  $\times$   $8.4^\circ$  (height). Stimulus presentation was locked to the refresh rate of the BOLDscreen monitor, which was nearly exactly 120 Hz. Empirically, we confirmed that the durations of runs were highly reliable, ranging from 427.94 s to 427.96 s. Throughout each run (including blank trials), a small semi-transparent fixation dot with a black border ( $0.2^\circ \times 0.2^\circ$ , 50% opacity) was present at the center of the stimuli. Every 1.4 s, the luminance of the dot was randomly set to one

of five different linearly spaced levels (0.17, 0.37, 0.58, 0.79, 1), with consecutive repetitions allowed. Stimuli were shown against a gray background (luminance level 0.5).

The fixation task (odd runs) was intended to be a challenging task that draws cognitive resources away from the stimuli and towards the small fixation dot (69). In the fixation task, subjects were instructed to fixate the central dot and to press button 1 using the index finger of their right hand when the dot darkens and button 2 using the middle finger of their right hand when the dot lightens. Subjects were informed that the dot brightness sometimes stays constant. Subjects were encouraged to ignore the stimulus images and focus on the color of the dot.

The one-back task (even runs) was intended to encourage perception of the stimuli. In the one-back task, subjects were instructed to fixate the central dot (ignoring the dot color changes) and to press button 1 if the presented image is different from the previous image and button 2 if the presented image is identical to the previous image. In a sense, this task is similar to the continuous recognition task performed in NSD-core where subjects were asked to judge whether each presented image is new (not yet seen) or old (presented before). Subjects were warned that some images may look degraded, noisy, or abstract, that some images may be positioned off to the side, and that some images may be quite similar but not identical to others. Subjects were additionally instructed to continue to fixate and wait for the next image in the event of blank trials.

## Summary of image repetitions and trial counts

Across the entire NSD-synthetic experiment, there are a total of 93 stimulus trials  $\times$  8 runs = 744 stimulus trials. Of these stimulus trials, 80 trials are one-back trials (10.8%). Considering all trials except the one-back trials, 268 images are presented 1 time per task and 16 images are presented 4 times per task. Considering all trials including the one-back trials, 236 images are presented 1 time per task, 32 images are presented 2 times per task, 8 images are presented 4 times per task, and 8 images are presented 5 times per task.

## Pre-processing of MRI data

Details on MRI pre-processing are provided in the Supplementary Information of NSD-core's paper (1). In brief, T1-weighted anatomical data were processed using FreeSurfer to create cortical surface representations. Functional data were pre-processed using one temporal resampling to correct for slice time differences and one spatial resampling to correct for head motion within and across scan sessions, EPI distortion, and gradient nonlinearities. Two versions of the functional data were prepared: a 1.8-mm standard-resolution preparation (temporal resolution 1.333 s) and an upsampled 1.0-mm high-resolution preparation (temporal resolution 1.000 s). Population receptive field and functional localizer experiments included in NSD were used to define retinotopic and category-selective regions of interest (ROIs), respectively. The defined ROIs include retinotopic visual areas (V1, V2, V3, hV4) as well as category-selective regions such as extrastriate body area (EBA), fusiform face area (FFA), parahippocampal place area (PPA), and visual word form area (VWFA).

## GLM analysis of fMRI data

We performed a GLM analysis of NSD-synthetic's pre-processed time-series data. This GLM analysis was the same as performed for NSD-core, and provides single-trial BOLD response

amplitude estimates ('betas') in units of percent signal change. Our GLM approach combines three analysis components: a library of hemodynamic response functions (HRFs), adaptation of the GLMdenoise technique (70, 71) to a single-trial GLM framework, and application of ridge regression (72) as a method for dampening the noise inflation caused by correlated single-trial GLM regressors. The GLM approach has been implemented in a software tool called GLMsingle (73).

In implementing the GLM analysis for NSD-synthetic, we made the following design choices. First, the fixation and one-back tasks were treated separately. Hence, each image was associated with two distinct conditions: one condition reflects the presentation of the image during the fixation task and the other condition reflects the presentation of the image during the one-back task. Second, because the GLMdenoise and ridge regression techniques require condition repeats (so that cross-validated optimization of hyperparameters can be performed), we designated certain groups of images as repeats of a single condition. This choice reflects the expectation that the images within each group are likely to give very similar evoked brain responses. We specifically designated each of image subclasses 1, 2, 3, and 27–71 as consisting of four images that are repeats of a single condition. Third, to minimize assumptions and avoid complications stemming from any repetition suppression (adaptation) effects, we separately coded the one-back trials such that each one-back trial was assigned its own single-trial regressor. As such, the responses evoked by the one-back trials have minimal influence on the optimization of the GLMdenoise and ridge regression analysis components.

## Analysis of behavioral data

For the fixation task, we extracted the first button response obtained within a time window extending 0–1,400 ms after each dot color change. We recorded whether the button response was correct (i.e., button 1 for brightness decrements, button 2 for brightness increments). We counted any case in which no button was pressed as an incorrect response. Percent correct was used to summarize performance.

For the one-back task, for each stimulus trial (excluding the first), we extracted the first button response obtained within a time window extending 250–4,250 ms after the onset of the stimulus image. We then interpreted the responses as reflecting a simple signal detection experiment. Trials in which the image was identical to the previously presented image (one-back trials) were treated as 'signal present' trials. For these trials, button 2 ("old") corresponds to a hit and button 1 ("new") corresponds to a miss. All other trials were treated as 'signal absent' trials. For these trials, button 2 ("old") corresponds to a false alarm and button 1 ("new") corresponds to a correct rejection. We counted any trial in which no button was pressed as an incorrect response (either a miss or a false alarm). Across trials, we computed the hit rate and the false alarm rate. We then converted these rates into the  $d'$  sensitivity index based on the inverse cumulative distribution function of the standard normal distribution. In this calculation, to prevent numerical explosion, we set the minimum and maximum possible values for the hit rate and false alarm rate to be 0.01 and 0.99, respectively.

## Analysis of fMRI data

Below, we describe the specific analyses of NSD demonstrated in this paper. These analyses go beyond the data preparation as described above. For all analyses we used the pre-processed fMRI betas version 3 ('nsdsyntheticbetas\_fithrf\_GLMdenoise\_RR' for NSD-synthetic and 'betas\_fithrf\_GLMdenoise\_RR' for NSD-core), prepared in FreeSurfer's fsaverage space. (Beta version 3 reflects all GLM analysis components as described above.) For the analyses shown in this paper, we interpret responses based on the presented stimuli, aggregating across the tasks performed by the subject.

To reduce the effect of noise on results, for each subject we utilized vertices with noise ceiling signal-to-noise ratio (ncsnr) scores above a threshold (except for the ncsnr visualization and for the encoding modeling, where we analyzed all available vertices). We quantified the ncsnr following the method proposed in NSD-core's data release paper (1), and selected 0.6 as the ncsnr threshold. We estimated the ncsnr independently for NSD-synthetic and NSD-core. Note that in the context of NSD-synthetic, we computed a single ncsnr estimate using fMRI responses from both tasks. Hence, our ncsnr estimate regards genuine task-related variability as noise, and may therefore underestimate signals in the data.

### Univariate fMRI response analysis

To compute NSD-synthetic's univariate fMRI responses, we sequentially averaged the fMRI responses across four dimensions: first across repeated trials (resulting in one trial-average response for each of the 284 NSD-synthetic stimulus images); second across vertices within each ROI (V1, V2, V3, hV4, PPA, VWFA); third across all images from the same subclass; and fourth across all subjects. This resulted in one univariate response for each image subclass and ROI, indicating the extent to which a given ROI is activated by each image subclass.

### Representational similarity analysis

Using representational similarity analysis (RSA) (41), we assessed the similarity of NSD-synthetic's multivariate fMRI responses between the ROIs of all subjects (V1, V2, V3, hV4, PPA, VWFA). We began by averaging the multivariate fMRI responses across repeated trials, resulting in one trial-average response for each of the 284 NSD-synthetic stimulus images. Next, for each ROI and subject, we built representational similarity matrices (RSMs), symmetric matrices indicating the similarity (Pearson's  $r$ ) of multivariate responses for each pair of stimulus images. Finally, for each pair of RSMs, we correlated (Pearson's  $r$ ) the lower triangle of the two RSMs. This resulted in one RSA score for each combination of subject and ROI, indicating the similarity of visual information encoded in their multivariate fMRI responses.

### Multidimensional scaling

To compare NSD-synthetic's and NSD-core's data distributions, we applied multidimensional scaling (MDS) (42, 43) to single-trial fMRI responses aggregated across the two datasets. This MDS analysis determines a low-dimensional space that best approximates the similarity of responses between all image pairs. To improve stability of results, we appended fMRI vertex responses across subjects before applying MDS. Furthermore, to assess potential differences in distributions due to session effects (e.g., incidental differences in overall fMRI response magnitude across sessions), we aggregated the 744 single-trial fMRI responses from NSD-synthetic to the



first 744 (out of 750) single-trial fMRI responses from two NSD-core scan sessions (sessions 10 and 20). The MDS analysis ultimately produced a two-dimensional array of shape (2,232 trials  $\times$  2 embedding dimensions).

We also applied MDS on only NSD-synthetic's fMRI responses (without NSD-core). To improve stability of results, for each of the 284 images we averaged the fMRI responses across repeated trials and appended vertex responses across subjects. This MDS analysis resulted in a two-dimensional array of shape (284 images  $\times$  2 embedding dimensions).

## Encoding models

We trained and tested encoding models that linearly map stimulus image features onto fMRI responses. The image features consisted of the layer-wise activations of four deep neural networks, all trained on the ILSVRC-2012 image set (74). The first deep neural network was AlexNet, a convolutional neural network pretrained on image classification (48), for which we used the activations from the output of the last sublayer of each of the eight model layers. The second deep neural network was vit\_b\_32, a vision transformer pretrained on image classification (49), for which we used the activations from the output of the last sublayer of each of the twelve model layers. The third deep neural network was ResNet-50 (50), a recurrent convolutional neural network pretrained on task-supervised image classification, for which we used the activations from the output of the last sublayer of each of the four model layers. The fourth deep neural network was MoCo (51), consisting of the same ResNet-50 architecture but trained with self-supervised contrastive learning, for which we used the activations from the output of the last sublayer of each of the four model layers.

We trained an independent encoding model using the image features of each deep neural network. The train data split consisted of NSD-core's 9,000 subject-unique images and corresponding fMRI responses (i.e., the images uniquely seen by individual subjects). During training, we first pre-processed each image by center-cropping it to square size using as size the image's smallest dimension; resized it to 224  $\times$  224 pixels; applied a square-root transformation to the RGB values if necessary (we used NSD-core images as-is and applied a square root transformation to NSD-synthetic images to match the NSD-core images); scaled its values to the range [0, 1]; and normalized the scaled RGB values using mean = [0.485, 0.456, 0.406] and standard deviation = [0.229, 0.224, 0.225]. We then fed each of the pre-processed train images to one of the four deep neural networks described above, and extracted the corresponding image features. Next, to reduce computational costs while retaining the most important axes of variation, we reduced the dimensionality of the concatenated features to 250 principal components using principal components analysis (PCA) (75). Finally, we trained independent linear regressions that mapped these PCA-reduced features onto the fMRI responses of each vertex in each subject.

We tested these encoding models both in-distribution (ID) and out-of-distribution (OOD). For ID, we tested models on 284 of the 515 NSD-core shared images that all subjects saw three times. For OOD, we tested models on NSD-synthetic's 284 stimulus images. For both the ID and OOD testing images, we used the same procedure described above for obtaining PCA-reduced features, and then mapped these features onto fMRI responses using the trained encoding models weights. This generated predicted responses for ID and OOD testing images for all vertices and subjects.

To assess the encoding models' ID and OOD generalization performance, we compared the predicted fMRI responses with their recorded (i.e., experimentally collected) counterparts, using Pearson's correlation. We correlated predicted and recorded fMRI responses independently for each vertex and subject, across the 284 ID or 284 OOD images, resulting in both ID and OOD correlation scores for each vertex and subject. These correlation scores reflect encoding model generalization performance, but are also affected by the level of noise in the recorded fMRI responses (which might not be equal between ID and OOD fMRI responses). Thus, to make the ID and OOD explained variance scores directly comparable, we normalized the ID and OOD generalization performance by the noise ceiling of the corresponding recorded fMRI responses. First, we squared all correlation scores after setting negative scores to zero, thus obtaining explained variance ( $r^2$ ) for each vertex and subject. Second, following the method proposed in NSD-core's data release paper (1), we computed each vertex's noise ceiling signal-to-noise ratio (ncsnr), independently for NSD-synthetic and NSD-core's test fMRI responses. We converted these ncsnr scores into noise ceiling scores indicating the amount of variance contributed by the signal expressed as a percentage of the total amount of variance in the data. These noise ceilings indicate the upper bound of model performance, given the noise in the data. Third, we divided the  $r^2$  ID and OOD scores with the corresponding noise ceilings. This resulted in noise-ceiling-normalized explained variance scores that indicate the amount of explainable variance that is accounted for by the models, for each vertex and subject.

## References

1. E. J. Allen, G. St-Yves, Y. Wu, J. L. Breedlove, J. S. Prince, L. T. Dowdle, M. Nau, B. Caron, F. Pestilli, I. Charest, J. B. Hutchinson, T. Naselaris, K. Kay, A massive 7T fMRI dataset to bridge cognitive neuroscience and artificial intelligence. *Nat. Neurosci.* **25**, 116–126 (2022).
2. A. T. Gifford, K. Dwivedi, G. Roig, R. M. Cichy, A large and rich EEG dataset for modeling human visual object recognition. *NeuroImage* **264**, 119754 (2022).
3. M. N. Hebart, O. Contier, L. Teichmann, A. H. Rockter, C. Y. Zheng, A. Kidder, A. Corriveau, M. Vaziri-Pashkam, C. I. Baker, THINGS-data, a multimodal collection of large-scale datasets for investigating object representations in human brain and behavior. *eLife* **12**, e82580 (2023).
4. E. R. Kupers, T. Knaben, E. P. Merriam, K. N. Kay, Principles of intensive human neuroimaging. *Trends Neurosci.* **47**, 856–864 (2024).
5. B. Lahner, K. Dwivedi, P. Iamshchinina, M. Graumann, A. Lascelles, G. Roig, A. T. Gifford, B. Pan, S. Jin, N. A. Ratan Murty, K. Kay, A. Oliva, R. Cichy, Modeling short visual events through the BOLD moments video fMRI dataset and metadata. *Nat. Commun.* **15**, 6241 (2024).
6. T. Naselaris, E. Allen, K. Kay, Extensive sampling for complete models of individual brains. *Curr. Opin. Behav. Sci.* **40**, 45–51 (2021).
7. P. Papale, F. Wang, M. W. Self, P. R. Roelfsema, An extensive dataset of spiking activity to reveal the syntax of the ventral stream. *Neuron*, S089662732400881X (2025).
8. R. M. Cichy, D. Kaiser, Deep Neural Networks as Scientific Models. *Trends Cogn. Sci.* **23**, 305–317 (2019).
9. A. Doerig, R. P. Sommers, K. Seeliger, B. Richards, J. Ismael, G. W. Lindsay, K. P. Kording, T. Konkle, M. A. J. Van Gerven, N. Kriegeskorte, T. C. Kietzmann, The neuroconnectionist research programme. *Nat. Rev. Neurosci.* **24**, 431–450 (2023).
10. T. C. Kietzmann, P. McClure, N. Kriegeskorte, “Deep Neural Networks in Computational Neuroscience” in *Oxford Research Encyclopedia of Neuroscience* (Oxford University Press, 2019); <https://oxfordre.com/neuroscience/view/10.1093/acrefore/9780190264086.001.0001/acrefore-9780190264086-e-46>).
11. B. A. Richards, T. P. Lillicrap, P. Beaudoin, Y. Bengio, R. Bogacz, A. Christensen, C. Clopath, R. P. Costa, A. De Berker, S. Ganguli, C. J. Gillon, D. Hafner, A. Kepecs, N. Kriegeskorte, P. Latham, G. W. Lindsay, K. D. Miller, R. Naud, C. C. Pack, P. Poirazi, P. Roelfsema, J. Sacramento, A. Saxe, B. Scellier, A. C. Schapiro, W. Senn, G. Wayne, D. Yamins, F. Zenke, J. Zylberberg, D. Therien, K. P. Kording, A deep learning framework for neuroscience. *Nat. Neurosci.* **22**, 1761–1770 (2019).
12. A. Saxe, S. Nelli, C. Summerfield, If deep learning is the answer, what is the question? *Nat. Rev. Neurosci.* **22**, 55–67 (2021).
13. D. L. K. Yamins, J. J. DiCarlo, Using goal-driven deep learning models to understand sensory cortex. *Nat. Neurosci.* **19**, 356–365 (2016).
14. A. T. Gifford, B. Lahner, S. Saba-Sadiya, M. G. Vilas, A. Lascelles, A. Oliva, K. Kay, G. Roig, R. M. Cichy, The Algonauts Project 2023 Challenge: How the Human Brain Makes Sense of Natural Scenes. arXiv [Preprint] (2023). <https://doi.org/10.48550/ARXIV.2301.03198>.
15. M. Schrimpf, J. Kubilius, H. Hong, N. J. Majaj, R. Rajalingham, E. B. Issa, K. Kar, P. Bashivan, J. Prescott-Roy, F. Geiger, K. Schmidt, D. L. K. Yamins, J. J. DiCarlo, Brain-Score: Which Artificial Neural Network for Object Recognition is most Brain-Like? [Preprint] (2018). <https://doi.org/10.1101/407007>.
16. C. Conwell, J. S. Prince, K. N. Kay, G. A. Alvarez, T. Konkle, A large-scale examination of inductive biases shaping high-level visual representation in brains and machines. *Nat. Commun.* **15**, 9383 (2024).
17. A. Doerig, T. C. Kietzmann, E. Allen, Y. Wu, T. Naselaris, K. Kay, I. Charest, Semantic scene descriptions as an objective of human vision. arXiv [Preprint] (2022). <https://doi.org/10.48550/ARXIV.2209.11737>.
18. M. Khosla, N. A. Ratan Murty, N. Kanwisher, A highly selective response to food in human

- visual cortex revealed by hypothesis-free voxel decomposition. *Curr. Biol.* **32**, 4159-4171.e9 (2022).
19. N. Jain, A. Wang, M. M. Henderson, R. Lin, J. S. Prince, M. J. Tarr, L. Wehbe, Selectivity for food in human ventral visual cortex. *Commun. Biol.* **6**, 175 (2023).
  20. G. St-Yves, E. J. Allen, Y. Wu, K. Kay, T. Naselaris, Brain-optimized deep neural network models of human visual areas learn non-hierarchical representations. *Nat. Commun.* **14**, 3329 (2023).
  21. J. S. Prince, G. A. Alvarez, T. Konkle, Contrastive learning explains the emergence and function of visual category-selective regions. *Sci. Adv.* **10**, eadl1776 (2024).
  22. J. Liu, Z. Shen, Y. He, X. Zhang, R. Xu, H. Yu, P. Cui, Towards Out-Of-Distribution Generalization: A Survey. arXiv [Preprint] (2021). <https://doi.org/10.48550/ARXIV.2108.13624>.
  23. S. Madan, W. Xiao, M. Cao, H. Pfister, M. Livingstone, G. Kreiman, Benchmarking Out-of-Distribution Generalization Capabilities of DNN-based Encoding Models for the Ventral Visual Cortex. arXiv [Preprint] (2024). <https://doi.org/10.48550/ARXIV.2406.16935>.
  24. T. Golan, P. C. Raju, N. Kriegeskorte, Controversial stimuli: Pitting neural networks against each other as models of human cognition. *Proc. Natl. Acad. Sci.* **117**, 29330–29337 (2020).
  25. Y. Ren, P. Bashivan, How well do models of visual cortex generalize to out of distribution samples? *PLOS Comput. Biol.* **20**, e1011145 (2024).
  26. J. J. DiCarlo, D. Zoccolan, N. C. Rust, How Does the Brain Solve Visual Object Recognition? *Neuron* **73**, 415–434 (2012).
  27. P. E. Downing, Y. Jiang, M. Shuman, N. Kanwisher, A Cortical Area Selective for Visual Processing of the Human Body. *Science* **293**, 2470–2473 (2001).
  28. R. Epstein, N. Kanwisher, A cortical representation of the local visual environment. *Nature* **392**, 598–601 (1998).
  29. K. Grill-Spector, Z. Kourtzi, N. Kanwisher, The lateral occipital complex and its role in object recognition. *Vision Res.* **41**, 1409–1422 (2001).
  30. N. Kanwisher, Functional specificity in the human brain: A window into the functional architecture of the mind. *Proc. Natl. Acad. Sci.* **107**, 11163–11170 (2010).
  31. N. Kanwisher, J. McDermott, M. M. Chun, The Fusiform Face Area: A Module in Human Extrastriate Cortex Specialized for Face Perception. *J. Neurosci.* **17**, 4302–4311 (1997).
  32. K. H. Foster, J. P. Gaska, M. Nagler, D. A. Pollen, Spatial and temporal frequency selectivity of neurones in visual cortical areas V1 and V2 of the macaque monkey. *J. Physiol.* **365**, 331–363 (1985).
  33. J. A. Movshon, I. D. Thompson, D. J. Tolhurst, Spatial and temporal contrast sensitivity of neurones in areas 17 and 18 of the cat's visual cortex. *J. Physiol.* **283**, 101–120 (1978).
  34. D. H. Hubel, T. N. Wiesel, Receptive fields and functional architecture of monkey striate cortex. *J. Physiol.* **195**, 215–243 (1968).
  35. S. Engel, X. Zhang, B. Wandell, Colour tuning in human visual cortex measured with functional magnetic resonance imaging. *Nature* **388**, 68–71 (1997).
  36. B. D. McCandliss, L. Cohen, S. Dehaene, The visual word form area: expertise for reading in the fusiform gyrus. *Trends Cogn. Sci.* **7**, 293–299 (2003).
  37. G. M. Boynton, J. B. Demb, G. H. Glover, D. J. Heeger, Neuronal basis of contrast discrimination. *Vision Res.* **39**, 257–269 (1999).
  38. R. L. De Valois, D. G. Albrecht, L. G. Thorell, Spatial frequency selectivity of cells in macaque visual cortex. *Vision Res.* **22**, 545–559 (1982).
  39. K. H. Foster, J. P. Gaska, M. Nagler, D. A. Pollen, Spatial and temporal frequency selectivity of neurones in visual cortical areas V1 and V2 of the macaque monkey. *J. Physiol.* **365**, 331–363 (1985).
  40. J. Ha, W. F. Broderick, K. Kay, J. Winawer, Spatial Frequency Maps in Human Visual Cortex: A Replication and Extension. Neuroscience [Preprint] (2025). <https://doi.org/10.1101/2025.01.21.634150>.
  41. N. Kriegeskorte, M. Mur, P. A. Bandettini, Representational similarity analysis - connecting the branches of systems neuroscience. *Front. Syst. Neurosci.* **2** (2008).
  42. M. L. Davison, S. G. Sireci, "Multidimensional Scaling" in *Handbook of Applied Multivariate Statistics and Mathematical Modeling* (Elsevier, 2000);

- <https://linkinghub.elsevier.com/retrieve/pii/B9780126913606500136>), pp. 323–352.
43. M. C. Hout, M. H. Papesh, S. D. Goldinger, Multidimensional scaling. *WIREs Cogn. Sci.* **4**, 93–103 (2013).
  44. K. N. Kay, T. Naselaris, R. J. Prenger, J. L. Gallant, Identifying natural images from human brain activity. *Nature* **452**, 352–355 (2008).
  45. N. Kriegeskorte, P. K. Douglas, Interpreting encoding and decoding models. *Curr. Opin. Neurobiol.* **55**, 167–179 (2019).
  46. T. Naselaris, K. N. Kay, S. Nishimoto, J. L. Gallant, Encoding and decoding in fMRI. *NeuroImage* **56**, 400–410 (2011).
  47. M. C.-K. Wu, S. V. David, J. L. Gallant, Complete Functional Characterization Of Sensory Neurons By System Identification. *Annu. Rev. Neurosci.* **29**, 477–505 (2006).
  48. A. Krizhevsky, One weird trick for parallelizing convolutional neural networks. arXiv [Preprint] (2014). <https://doi.org/10.48550/ARXIV.1404.5997>.
  49. A. Dosovitskiy, L. Beyer, A. Kolesnikov, D. Weissenborn, X. Zhai, T. Unterthiner, M. Dehghani, M. Minderer, G. Heigold, S. Gelly, J. Uszkoreit, N. Houlsby, An Image is Worth 16x16 Words: Transformers for Image Recognition at Scale. arXiv [Preprint] (2020). <https://doi.org/10.48550/ARXIV.2010.11929>.
  50. K. He, X. Zhang, S. Ren, J. Sun, “Deep Residual Learning for Image Recognition” in *2016 IEEE Conference on Computer Vision and Pattern Recognition (CVPR)* (IEEE, Las Vegas, NV, USA, 2016; <http://ieeexplore.ieee.org/document/7780459/>), pp. 770–778.
  51. K. He, H. Fan, Y. Wu, S. Xie, R. Girshick, “Momentum Contrast for Unsupervised Visual Representation Learning” in *2020 IEEE/CVF Conference on Computer Vision and Pattern Recognition (CVPR)* (IEEE, Seattle, WA, USA, 2020; <https://ieeexplore.ieee.org/document/9157636/>), pp. 9726–9735.
  52. J. Zbontar, L. Jing, I. Misra, Y. LeCun, S. Deny, Barlow Twins: Self-Supervised Learning via Redundancy Reduction. arXiv [Preprint] (2021). <https://doi.org/10.48550/ARXIV.2103.03230>.
  53. K. N. Kay, Principles for models of neural information processing. *NeuroImage* **180**, 101–109 (2018).
  54. T. Konkle, G. A. Alvarez, A self-supervised domain-general learning framework for human ventral stream representation. *Nat. Commun.* **13**, 491 (2022).
  55. A. Doerig, R. P. Sommers, K. Seeliger, B. Richards, J. Ismael, G. W. Lindsay, K. P. Kording, T. Konkle, M. A. J. Van Gerven, N. Kriegeskorte, T. C. Kietzmann, The neuroconnectionist research programme. *Nat. Rev. Neurosci.* **24**, 431–450 (2023).
  56. K. Kay, K. Bonnen, R. N. Denison, M. J. Arcaro, D. L. Barack, Tasks and their role in visual neuroscience. *Neuron* **111**, 1697–1713 (2023).
  57. J. Zhou, N. C. Benson, K. N. Kay, J. Winawer, Compressive Temporal Summation in Human Visual Cortex. *J. Neurosci.* **38**, 691–709 (2018).
  58. A. T. Gifford, D. Bersch, M. St-Laurent, B. Pinsard, J. Boyle, L. Bellec, A. Oliva, G. Roig, R. M. Cichy, The Algonauts Project 2025 Challenge: How the Human Brain Makes Sense of Multimodal Movies. arXiv [Preprint] (2025). <https://doi.org/10.48550/ARXIV.2501.00504>.
  59. J. Boyle, B. Pinsard, V. Borghesani, F. Paugam, E. DuPre, P. Bellec, “The Courtois NeuroMod project: quality assessment of the initial data release (2020)” in *2023 Conference on Cognitive Computational Neuroscience* (Cognitive Computational Neuroscience, Oxford, UK, 2023; [https://2023.ccneuro.org/view\\_paper.php?PaperNum=1602](https://2023.ccneuro.org/view_paper.php?PaperNum=1602)).
  60. G. Shen, T. Horikawa, K. Majima, Y. Kamitani, Deep image reconstruction from human brain activity. *PLOS Comput. Biol.* **15**, e1006633 (2019).
  61. F. L. Cheng, T. Horikawa, K. Majima, M. Tanaka, M. Abdelhack, S. C. Aoki, J. Hirano, Y. Kamitani, Reconstructing visual illusory experiences from human brain activity. *Sci. Adv.* **9**, ead3906 (2023).
  62. G. A. Rousselet, M. J.-M. Macé, M. Fabre-Thorpe, Is it an animal? Is it a human face? Fast processing in upright and inverted natural scenes. *J. Vis.* **3**, 5 (2003).
  63. C. M. Mooney, Age in the development of closure ability in children. *Can. J. Psychol. Rev. Can. Psychol.* **11**, 219–226 (1957).
  64. D. B. Walther, B. Chai, E. Caddigan, D. M. Beck, L. Fei-Fei, Simple line drawings suffice for functional MRI decoding of natural scene categories. *Proc. Natl. Acad. Sci.* **108**, 9661–9666

- (2011).
65. J. J. D. Singer, R. M. Cichy, M. N. Hebart, The Spatiotemporal Neural Dynamics of Object Recognition for Natural Images and Line Drawings. *J. Neurosci.* **43**, 484–500 (2023).
  66. W. F. Broderick, E. P. Simoncelli, J. Winawer, Mapping spatial frequency preferences across human primary visual cortex. *J. Vis.* **22**, 3 (2022).
  67. D. I. A. MacLeod, R. M. Boynton, Chromaticity diagram showing cone excitation by stimuli of equal luminance. *J. Opt. Soc. Am.* **69**, 1183 (1979).
  68. A. Stockman, D. I. A. MacLeod, N. E. Johnson, Spectral sensitivities of the human cones. *J. Opt. Soc. Am. A* **10**, 2491 (1993).
  69. K. N. Kay, J. D. Yeatman, Bottom-up and top-down computations in word- and face-selective cortex. *eLife* **6**, e22341 (2017).
  70. K. N. Kay, A. Rokem, J. Winawer, R. F. Dougherty, B. A. Wandell, GLMdenoise: a fast, automated technique for denoising task-based fMRI data. *Front. Neurosci.* **7** (2013).
  71. I. Charest, N. Kriegeskorte, K. N. Kay, GLMdenoise improves multivariate pattern analysis of fMRI data. *NeuroImage* **183**, 606–616 (2018).
  72. A. Rokem, K. Kay, Fractional ridge regression: a fast, interpretable reparameterization of ridge regression. *GigaScience* **9**, giaa133 (2020).
  73. J. S. Prince, I. Charest, J. W. Kurzawski, J. A. Pyles, M. J. Tarr, K. N. Kay, Improving the accuracy of single-trial fMRI response estimates using GLMsingle. *eLife* **11**, e77599 (2022).
  74. O. Russakovsky, J. Deng, H. Su, J. Krause, S. Satheesh, S. Ma, Z. Huang, A. Karpathy, A. Khosla, M. Bernstein, A. C. Berg, L. Fei-Fei, ImageNet Large Scale Visual Recognition Challenge. *Int. J. Comput. Vis.* **115**, 211–252 (2015).
  75. J. P. Cunningham, B. M. Yu, Dimensionality reduction for large-scale neural recordings. *Nat. Neurosci.* **17**, 1500–1509 (2014).

## Acknowledgements

We thank J. Bosten, B. Broderick, and A. White for consultation regarding stimulus design. We also thank E. Allen and Y. Wu for collecting the neuroimaging data, and the HPC Service of FUB-IT, Freie Universität Berlin for computing time (DOI: <http://dx.doi.org/10.17169/refubium-26754>).

## Funding

Collection of the NSD dataset was supported by NSF IIS-1822683 (K.K.) and NSF IIS-1822929 (T.N.). This work was supported by NIH grant R01EY034118 (K.K.), German Research Council (DFG) grants (CI 241/1-3, CI 241/1-7, INST 272/297-1) (R.M.C.), and European Research Council (ERC) starting grant (ERC-StG-2018-803370) (R.M.C.).

## Author contributions

K.K. designed the experiment and pre-processed the data. A.T.G. modeled and analyzed the data. K.K. and A.T.G. prepared figures. A.T.G., K.K., T.N., and R.M.C. interpreted results. A.T.G. and K.K. wrote the manuscript. All authors discussed and edited the manuscript.

## Competing interests

The authors declare no competing interests.

## Data and materials availability

The NSD-synthetic dataset is freely available at <http://naturalscenesdataset.org>. We provide both raw data in BIDS format and prepared data files, along with extensive technical documentation in the NSD Data Manual ([https://cvnlab.slite.page/p/CT9Fwl4\\_hc/NSD-Data-Manual](https://cvnlab.slite.page/p/CT9Fwl4_hc/NSD-Data-Manual)). We provide an archive of code used for creating the NSD dataset (<https://github.com/cvnlab/nsddatapaper/>). We also provide utility functions for working with the prepared NSD data (<https://github.com/cvnlab/nsdcode/>). Finally, we provide code to reproduce the analyses of the NSD data shown in this paper (<https://github.com/gifale95/NSD-synthetic>).